nature geoscience

Supplementary information

https://doi.org/10.1038/s41561-024-01465-7

Tipping point in ice-sheet grounding-zone melting due to ocean water intrusion

In the format provided by the authors and unedited

Contents

1 Coupled layered intrusion-melt model

In this section, we describe the coupled layered intrusion-melt model referred to in the main text. The setup is shown schematically in figure 1.

1.1 Layered intrusion model

The layered intrusion model is as described by [1] and [2], albeit with a variable channel thickness. The 'along grounding zone' (transverse) average behaviour of the subglacial hydrological system is considered as a two layer system in which cold, fresh subglacial discharge from upstream of the grounding zone is underlain by warm, saline ocean water. These two layers are treated as immiscible (except for the exchange of heat and salt, see below). The grounding zone is inclined at an angle θ to the horizontal, along which the x-axis is aligned. The layer-averaged velocity and thickness of the warm and cold layers are denoted by $u_i(x,t)$ and $h_i(x,t)$ for $i = 1, 2$, respectively (supplementary figure 1). Far upstream of the grounding zone, the subglacial network is assumed to have an average thickness H_∞ and fresh water flow velocity U_∞. Conservation of mass of the two layers is expressed by

$$\frac{\partial h_1}{\partial t} + \frac{\partial}{\partial x}(u_1 h_1) = 0, \tag{1}$$

$$\frac{\partial h_2}{\partial t} + \frac{\partial}{\partial x}(u_2 h_2) = 0, \tag{2}$$

where $h = h_1 + h_2$ is the total channel thickness, and $q_i = h_i u_i$, $i = 1, 2$ is the flux in layer i. Note that (1)–(2) results from assuming negligible fresh water input via melting into the fresh water layer. Although melting is important in altering the thickness of the subglacial channel, the water input due to this melting is insignificant compared to the flux of water from upstream. For example, a typical value of the upstream subglacial flux is $U_\infty H_\infty \approx 10^{-3}$ m^2 s^{-1}, while the total input from melting is on the order of $\int \dot{m} \approx 10^{-4}$m^2 s^{-1}, where the integral is taken over the horizontal lengthscale. (More generally, taking the horizontal lengthscale H_∞/c_d as identified below, the ratio between upstream subglacial flux and total input from melting is on the order of $\mathrm{St}c/\mathcal{L}\Delta T/c_d \sim 10^{-2}$, where variables are as defined in the main text.)

Momentum conservation in each layer requires

$$\frac{\partial u_1}{\partial t} + u_1\frac{\partial u_1}{\partial x} + \frac{1}{\rho}\frac{\partial P}{\partial x} + \frac{c_i|u_1 - u_2|(u_1 - u_2)}{h_1} + \frac{c_d u_1^2}{h_1} = 0, \tag{3}$$

$$\frac{\partial u_2}{\partial t} + u_2\frac{\partial u_2}{\partial x} + \frac{1}{\rho}\frac{\partial P}{\partial x} - \frac{c_i|u_1 - u_2|(u_1 - u_2)}{h_2} + \frac{c_d u_2^2}{h_2} + g'\left(\frac{\partial h_2}{\partial x} + \tan\theta\right) = 0. \tag{4}$$

where P is the barotropic pressure within the channel, c_i is the coefficient of interfacial drag between the two layers, and c_d is the coefficient of wall drag. These two drag coefficients parametrize the behaviour in the transverse (along grounding line) direction, with high values of c_d corresponding to strong wall-fluid interactions (and vice versa for low c_d) and high values of c_i corresponding to strong resistance between the layers. In (3)–(4), $g' = g\Delta\rho/\rho_0$ is the reduced gravity, with g the gravitational acceleration, $\Delta\rho$ the density difference between the two layers, and ρ_0 a reference density. We assume that the density difference between the two layers is constant.

For a given channel thickness $h(x,t)$, the system (1)–(4), alongside the geometric constraint $h = h_1 + h_2$, are a system of five equations for the five unknowns u_1, u_2, h_1, h_2, and P. This system is closed with boundary conditions: firstly, the thickness and velocity of the upstream subglacial hydrological network are prescribed:

$$u_1 = U_\infty, \qquad h_1 = H_\infty \qquad \text{as } x \to -\infty. \tag{5}$$

Secondly, the upper-layer must be at the subcritical-to-supercritical transition at the channel entrance [2]

$$\frac{u_1}{\sqrt{g'h_1}} = 1 \qquad \text{at } x = 0. \tag{6}$$

The boundary condition (6) arises because the freshwater flow becomes unconfined as it leaves the region and hence its behaviour is expected to transition from subcritical to supercritical there (see [2] for a full description of this boundary condition).

Following [2] and [1], the system (1)–(4) is simplified by making the assumption that the flow in both layers flow is steady (i.e. all time derivatives in (1)–(4) are ignored). Unlike the models of [2] and [1], our model has another timescale in it, namely that on which the confining channel geometry changes. The relevant timescale for flow in the channel (of a given width) to reach equilibrium is the advective timescale $\mathbf{L}/U_\infty$, where $\mathbf{L} = H_\infty/c_d$ is the lengthscale of the channel, while the timescale over which the geometry evolves (see §1.3 below) is the ice advection timescale $\mathbf{L}/V$. This latter timescale is typically 10^4 times larger than the former, so it is reasonable to treat the hydraulic equations (3)–(4) as quasi-steady. A result of assuming this quasi-steady state is that the average velocity of the lower layer must be zero ($u_2 = 0$). (In fact, there is likely some recirculation of fluid within the lower layer – inwards along the bottom and outwards along the top – but there is no net horizontal flow.)

Noting that the flux of fluid in the fresh layer is constant as a result of the quasi-steady assumption, i.e. $q_1 = u_1 h_1 = U_\infty H_\infty = q_\infty$), and taking the difference of (3)–(4) (in which the barotropic pressure gradient cancels out), we obtain a single ODE for h_1:

$$\left[\left(\frac{U_\infty}{\sqrt{g'h_1}}\right)^2 - 1\right]\frac{\partial h_1}{\partial x} = \left(\frac{U_\infty}{\sqrt{g'h_1}}\right)^2\left(c_d + c_i\frac{h}{h-h_1}\right) - \left(\tan\theta + \frac{\partial h}{\partial x}\right). \tag{7}$$

This equation is identical to that considered by [1], albeit that the channel width h is spatially and temporally variable and the upper layer thickness h_1 is temporally variable.

1.2 Melting and channel evolution

Flow through the grounding-zone feeds back on the channel shape via melting of the upper surface at a rate $\dot{m}(x,t)$. Since grounding zones are long and thin, this melt rate can reasonably be assumed to apply perpendicular to the basal slope.

We apply the so-called 'two equation formulation' for melting. The two equations refer to a liquidus condition and approximate heat balance,

$$T_f(\mathcal{S}, z_b) = T_{\text{ref}} + \lambda z_b - \Gamma \mathcal{S}, \tag{8}$$

$$\dot{m}\left\{L + c_s\left[T_f(\mathcal{S}, z_b) - T_i\right]\right\} = \text{St}u^* c\left[T - T_f(\mathcal{S}, z_b)\right], \tag{9}$$

respectively. Here $T_{\text{ref}} = 8.32 \times 10^{-2}$°C is a reference temperature, $\lambda = 7.61 \times 10^{-4}$°C m^{-1} is the liquidus slope with depth, $\Gamma = 5.73 \times 10^{-2}$°C is the liquidus slope with salinity, z_b is the local depth, $\mathcal{L} = 3.35 \times 10^5$ J kg^{-1} is the latent heat of fusion of seawater, $c_s = 2.009 \times 10^3$ J kg °C^{-1} is the specific heat capacity of ice, T_i is the internal ice temperature, u^* is the velocity outside a viscous boundary layer adjacent to the ice-ocean interface, $c = 3.974 \times 10^3$ J kg °C^{-1} is the specific heat capacity of water, and T and S are the temperature and salinity outside the viscous boundary layer, respectively. (Values quoted here are standard values, assumed constant, from [3, 4].) The Stanton number St is the ratio between the thermal flux into the ice-ocean interface and the thermal capacity of this fluid, which parametrizes exchange across a boundary layer at the ice-ocean interface [5]; mathematically, this can be expressed as $\text{St} = \mathcal{H}/(\rho u c)$, where $\mathcal{H}$ is the convective heat transfer coefficient, ρ is the fluid density, and u is the velocity of the fluid. We take the Stanton number to be constant, as is standard [e.g. 3, 6, 7].

Since the local freezing temperature and internal ice temperature are within a few degrees of each other, then $|T_f(\mathcal{S}, z_b) - T_i| \ll \mathcal{L}/c$ and the second of (9) can be approximated by

$$\mathcal{L}\dot{m} = \text{St}cu^*\tau, \tag{10}$$

where

$$\tau = T - T_f(\mathcal{S}, z_b) \tag{11}$$

is the local thermal driving. By dividing both sides of (10) by $\mathcal{L}$, we obtain equation (2) in the methods section of the main text.

We take the freshwater layer velocity, which is the layer adjacent to the ice-oceean interface, as the boundary layer velocity, i.e. $u^* = u_1$.

We take a simple model for the channel temperature and salinity, assuming that these quantities are equal to the depth-weighted average of the two layers:

$$T = \phi T_D + (1 - \phi) T_O, \tag{12}$$

$$\mathcal{S} = \phi \mathcal{S}_D + (1 - \phi) \mathcal{S}_O \tag{13}$$

where T_D and $\mathcal{S}_D$ are the temperature and salinity of the subglacial discharge layer, respectively, T_0 and $\mathcal{S}_0$ are the temperature and salinity of the ocean layer, and $\phi = \frac{h_1}{h}$ is the cross-channel fraction occupied by the freshwater layer.

We assume that the subglacial discharge layer consists entirely of freshwater at the local freezing point, and therefore take

$$S_d = 0, \tag{14}$$

$$T_D = T_{\text{ref}} + \lambda z_b. \tag{15}$$

Note that (15) arises from (14) in conjunction with the liquidus condition (8). Inserting (12)–(15) into (11), we obtain the thermal driving

$$\tau = (1-\phi)\left[T_O - T_D + \Gamma\mathcal{S}_O\right]. \tag{16}$$

To close the model, we must describe how the channel geometry responds to melting. With the assumption that the ice above the channel has constant velocity V (a reasonable assumption given the long, $\mathcal{O}(10\text{ s})$ kms on which ice sheet velocities vary), the kinematic boundary condition on the upper surface of the channel requires:

$$\frac{\partial h}{\partial t} + V\frac{\partial h}{\partial x} = \dot{m}. \tag{17}$$

As initial conditions, we take a configuration of parallel channel walls: $h(x, t = 0) = 1$, which is the configuration considered by [1] and [2]. We are primarily interested in the final configuration; as we show in §2, the steady solution, should it exist, is unique and therefore independent of the initial condition used.

With an initial condition specified, the timestepping process is as follows: for the given channel thickness $h(x, t)$, we use equation (7) to determine the freshwater water layer thickness h_1 (at the first timestep, when the channel walls are parallel, this is the solution described by [1] and [2]) and thus the thermal driving from (12). The freshwater layer velocity is then determined via conservation of mass ($h_1 u_1 = H_\infty U_\infty$) and the melt determined using (10). The thickness is then updated using (17), and the procedure repeated.

1.3 Non-dimensionalization

The problem (7), (10), (17) is non-dimensionalized by introducing dimensionless variables (denoted with hats):

$$\hat{h}_1 = \frac{h_1}{H_\infty}, \qquad \hat{h} = \frac{h}{H_\infty}, \qquad \hat{x} = \frac{c_d\, x}{H_\infty}, \qquad \hat{t} = \frac{t}{\mathcal{T}}. \tag{18}$$

The scales introduced are based on a horizontal lengthscale H_∞/c_d and the melting timescale $\mathcal{T} = H_\infty\mathcal{L}/(U_\infty \mathrm{St} c \Delta T)$, where $\Delta T = T_O + \Gamma\mathcal{S}_O - T_D$ is the thermal forcing.

After inserting dimensionless variables (18), the channel flow equation (7) becomes

$$\left(\frac{F^2}{\hat{h}_1^3} - 1\right)\frac{\partial \hat{h}_1}{\partial \hat{x}} = \frac{F^2}{\hat{h}_1^3}\left(1 + C\frac{h}{\hat{h} - \hat{h}_1}\right) - \left(S + \frac{\partial \hat{h}}{\partial \hat{x}}\right), \tag{19}$$

where $F = U_\infty/\sqrt{g' H_\infty}$ is the upstream Froude number, $S = \tan\theta/c_d$ is the rescaled bed slope, and $C = c_i/c_d$ is a rescaled drag coefficient.

After combining the melt model (10) and the kinematic condition (17), and inserting dimensionless variables (18), we obtain

$$\frac{\partial \hat{h}}{\partial \hat{t}} + \frac{1}{M}\frac{\partial \hat{h}}{\partial \hat{x}} = \frac{1}{\hat{h}_1}\left(1 - \frac{\hat{h}_1}{\hat{h}}\right) \tag{20}$$

where

$$M = \frac{U_\infty}{V}\frac{\mathrm{St}}{C_d}\frac{\Delta T}{\mathcal{L}/c} \tag{21}$$

is the dimensionless melt parameter.

The dimensionless boundary and initial conditions are

$$\hat{h}_1(\hat{x}=0,\hat{t})^{3/2} = F^{2/3} \tag{22}$$

and

$$\hat{h}(\hat{x},\hat{t}=0) = 1. \tag{23}$$

The dimensionless intrusion length, denoted $\hat{\ell}(\hat{t})$, is determined by the condition that $\hat{h} = \hat{h}_1$ at $\hat{x} = -\hat{\ell}(\hat{t})$. The final intrusion length, which is shown in figures 3–4 of the main text, is $L = \lim_{\hat{t}\to\infty}\hat{\ell}$.

1.4 Model simplifications and assumptions

In this section, we explicitly set out the simplifications and assumptions made in the model derivation, and briefly describe their impact on the behaviour of intrusions and on our results.

- **Flowline model:** The layered intrusion model of [1, 2] is effectively a flowline model, with the behaviour in the lateral (along grounding zone) direction (into the page in figure 1) parametrized by an effective drag coefficient. As mentioned in the main text, the boundary between bounded and unbounded intrusions is relatively insensitive to the value of this parameter, providing support for our use of a two-dimensional model. In practice, lateral heterogeneities in grounding-zone characteristics (e.g. subglacial hydrology and bed slope) and complex flow characteristics within ice shelf cavities (e.g. coriolis forces and bathymetric features) may lead to significant seawater intrusion at some parts of the ice-ocean interface but not others. High-resolution three-dimensional models of grounding zones are required to probe these effects in detail. In addition, incorporating a third-dimension into any eventual coupling with an ice-sheet will increase stability of the ice-sheet model, in general [8].
- **Ice velocity:** In our model, we assume a constant ice velocity V, which is reasonable since ice velocities typically vary on long (O(10s of kms)) lengthscales, relative to the intrusion length. It is important to note however, that ice velocity may act as a stabilizing mechanism on intrusion: an increase in grounding-zone melting (as a result of, for example, passing the bounded-unbounded intrusion tipping point) would be expected to result in ice acceleration, thereby effectively reducing the value of the parameter M and potentially stabilizing the intrusion. However, investigating

this mechanism in detail requires the use of a coupled model, which includes (at least) both ice and subglacial hydrology components. This study provides strong motivation for the development of such models.

- **Tides:** Characteristics of grounding zones can vary significantly on tidal timescales, as the tidal-flexure of ice shelves changes the geometry [9, 10, for example] and ocean conditions in grounding zones [11–13, for example]. The magnitude of tidal influence on grounding zones is not uniform, but can vary significantly, both within, and between different, ice shelves, and depending on the specific characteristics of the region [9]. Our model does not include tides: the timescale on which ice and ocean conditions respond to tides ($\mathcal{O}$(hours)) is typically much shorter than the timescale relevant to subglacial flow ($\mathcal{O}$(days)); as such, our model can be considered to be an average over the tidal cycle, with the grounding line slope and ocean conditions at their average value (note that the datasets used herein also reflect long term averages and can therefore also be considered as averages over the tidal cycle). Future work should consider the effect of tidal variations on seawater intrusions, and, in particular, seek to understand whether variations on the tidal timescale might integrate to a non-trivial effect on the longer timescale considered here. In section 3, we describe the results of a simple investigation into the effect of tides on seawater intrusion, in which tidal flexure modifies the boundary layer velocity uniformly through the channel on a tidal timescale. We find that for relatively small tidal velocity amplitudes (with respect to the upstream flow velocity), the behaviour is essentially the same as the no tides case, with the intrusion distance oscillating around the no-tide value on the tidal timescale. However, for relatively large tidal velocity amplitudes, tidal velocity fluctuations dominate, and result in increased intrusion over the no tides case. Importantly, we find that including tides in this way only enhances intrusion, i.e. makes the mechanism of grounding zone melting stronger. In addition, the tipping-point behaviour still exists, but the location of the bounded-unbounded intrusion boundary is modulated by the amplitude of tidal oscillations.
- **Constant Bed Slope:** The layered intrusion model assumes that the bedslope θ is constant. This is reasonable provided that the intrusion length is shorter than the lengthscale on which the bed changes significantly. On longer lengthscales, bed variations may act to suppress or promote intrusion: bedslopes with negative slope gradients ($\mathrm{d}\theta/\mathrm{d}x < 0$) will promote intrusion, while bedslopes with negative slope gradients ($\mathrm{d}\theta/\mathrm{d}x < 0$) will suppress intrusion.
- **Constant layer temperatures:** We assume that both warm and cold layers remain at their constant inflow temperatures, with no entrainment between the two layers and no freshwater input into the cold water layer. Our melt model, which considers the cross layer averaged temperature as that appropriate for melting, is a proxy for temperature mixing between the two layers, and, as discussed above, melt input into the channel is relatively small compared with channel through flow, justifying this assumption. Energy is provided to the system via the warm layer, with increasing amounts of energy required to sustain the melting provided by increasing warm water content via channel widening. It can be shown that relatively little energy provided by the warm layer is actually used for melting, further justifying

the assumption of a constant warm layer: the total heat flux into the cavity can be estimated as $Q = c\rho\mathcal{V}\Delta T$, where $\mathcal{V}$ is the volume flux of fluid (per unit width in the along grounding line direction) and other variables are as defined above. If all of this heat were used for melting, it would produce a melt flux on the order of $Q/(\mathcal{L}\rho) = c\mathcal{V}\Delta T/\mathcal{L}$. This can be compared with the channel integrated melt flux, which scales with $\mathrm{St}cu^*\Delta TL/H$, where L is the intrusion length. The ratio of these is $H/(L\mathrm{St})$ is on the order of 5 for a kilometer length intrusion (for which the channel width is on the order of 1 m, see figure 2 of the main text), i.e. there is typically much more heat available than that which is utilised for melting. This suggests that relatively little heat is lost to melting, justifying our use of a constant warm layer. We note however, that as the intrusion length L goes to infinity, this ratio decreases (the channel thickness H will increase to counter this, but this widening is also bounded). We thus expect that the warm water layer temperature would reduce as the intrusion length goes to infinity, potentially stabilizing the intrusion.

2 Steady intrusion length

In this section, we describe the procedure for determining the steady intrusion length L. Note that in this section, all variables are assumed dimensionless and hats are dropped.

2.1 Steady intrusion problem

To determine the steady intrusion length L for a given set of parameters (F, C, S, M), we consider the steady form of the coupled layered intrusion-melt equations (19)–(20), which read

$$\left(\frac{F^2}{h_1^3} - 1\right)\frac{\partial h_1}{\partial x} = \frac{F^2}{h_1^3}\left(1 + C\frac{h}{h - h_1}\right) - \left(S + \frac{\partial h}{\partial x}\right), \tag{24}$$

$$\frac{1}{M}\frac{\partial h}{\partial x} = \frac{1}{h_1}\left(1 - \frac{h_1}{h}\right). \tag{25}$$

If a steady solution with a bounded intrusion exists, it will necessarily have $h = h_1 = 1$ at $x = L$ and $h_1 = F^{2/3}$ at $x = 0$.

The idea is as follows: we begin by specifying an arbitrary finite interval $[x_l, x_u]$, where $x_u - x_l \gg 1$ and then integrate (24)–(25) forwards in x from $x = x_l$ towards $x = x_u$. Should the solution reach the sub-supercritical transition threshold (22) at a point $x = x_s \in [x_l, x_u]$, then the steady intrusion length is $L = x_s - x_l$. However, if the solution does not reach (22), there is no steady solution with a bounded intrusion length. The specific values x_u and x_l are arbitrary because the problem (24)–(25) is translationally invariant. In the results shown here, we take $x_u - x_l = 10^5$.

To avoid a singularity in the interfacial drag term that appears in the momentum equation (25) at the nose of the intrusion (where $h_1 = h$), we integrate (24)–(25) using a perturbed initial condition, based on an asymptotic expansion of the local solution,

$$h = 1 + \frac{2M}{3}\left(\frac{2CF^2}{1-F^2}\right)^{1/2} x_\epsilon^{3/2}, \tag{26}$$

$$h_1 = 1 - \left(\frac{2CF^2}{1-F^2}\right)^{1/2} x_\epsilon^{1/2}, \tag{27}$$

at $x = x_l + x_\epsilon$ where $x_\epsilon \ll 1$ (in the results shown here and in the main text, we used $x_\epsilon = 10^{-3}$, but found that results are insensitive to this value provided that $x_\epsilon \ll 1$).

In supplementary figure 2, we show the solution to (24)-(27) using the parameter values used to generate figure 2 of the main text and $x_l = 10^5$). This demonstrates the procedure: for the smaller value of M ($M = 0.27$, left panels in figure 2), the solution h_1 decreases monotonically from $h_1 = 1$ at $x = x_l$ to $h_1 = F^{2/3}$, which is attained at $x = x_s \approx 4$. Thus, this parameter set corresponds to a bounded intrusion, with a dimensional intrusion length of approximately 110m. For the larger value of M ($M = 0.3$, right panels in figure 2), h_1 initially decreases (inset in figure 2b) before reaching a local minimum at a value larger than $F^{2/3}$ and increasing monotonically thereafter. The termination value $h_1 = F^{2/3}$ is never attained.

This behaviour is generic: for $M < M_c$, the solution for h_1 always heads monotonically towards $h_1 = F^{2/3}$, attaining it in a finite distance, while for $M > M_c$, the solution attains a local minimum beyond which it increases without bound. It is possible to show – although it does not provide insight and is therefore not included here – that any solution of (24)–(25) has a unique local minimum and thus, if a local minimum with $h_1 > F^{2/3}$ is attained, the solution will never attain $h_1 = F^{2/3}$. This confirms that for $M > M_c$, no bounded, steady intrusion exists.

Note that if a steady intrusion length exsits, once the steady problem (24)–(25) has been solved numerically, the cold layer thickness h_1 and channel thickness h are known. The dimensionless melt rate can then be determined as $1/h_1(1 - h_1/h)$ (see equation (20)), and the dimensional melt rate reproduced by undoing the scalings of (18). This may form the basis for a parametrization of grounding zone melting, but we stress that it is only valid in the bounded intrusion regime.

2.2 Bisection algorithm for M_c

To determine the critical melt parameter M_c shown as the boundary between green and blue sections of figure 3 of the main text, we apply a bisection method. For a given (F, S, C), we first specify an upper M_c^u and lower M_c^l bound on M_c, determined as any value which result in unbounded and bounded intrusion, respectively. We then apply a standard bisection procedure: at each step, we take a candidate melt parameter as the mean of the current upper and lower bound value. The steady equations (24)–(25) are then solved using this value of M; if this value corresponds to unbounded (bounded, respectively) intrusion, it replaces the upper (lower) bound. This procedure is repeated until the difference between the upper and lower bounds is below a predetermined threshold (in those results shown here, this is 10^{-3}). Examples of the solutions h_1 generated during this procedure are shown in supplementary figure 3a.

The same procedure outlined in this section is applied to determine the critical slope S_c and critical Froude number F_c (noting that unbounded intrusion occurs for $F < F_c$ and thus the bisection algorithm must be adjusted accordingly). Examples of the h_1 generated during this procedure are shown in supplementary figure 3b (for S_c) and figure 3c (for F_c).

3 Investigating tidal influences on seawater intrusion

As an ice shelf cavity opens in response to tidal flexure, water will invade the newly-opened cavity and as the cavity closes, water will be evacuated. Given that tidal grounding line migrations may be on the order of kilometers [10], and tidal cycles are diurnal, this may result in rapid inflow and outflow of water into the cavity. Such high flow speeds have the potential to significantly affect the intrusion mechanism of interest here because flow speeds directly enter into the melt rate model (10).

The precise dynamics of such tidal flushing are poorly constrained. However, a simple way to investigate their effect on the seawater intrusion model considered here is to modify the boundary layer velocity appropriate for melting (equation (10)) to introduce a tidal component, i.e. setting

$$u^* = \left| u_1 + U_T \sin\left(\frac{2\pi t}{\tau_S}\right) \sin\left(\frac{2\pi t}{\tau_L}\right) \right|, \tag{28}$$

where U_T is the amplitude of the tidal velocity signal, $\tau_S = 12$ hours is the solar tidal period, $\tau_L = 28$ days is the lunar tidal period (supplementary figure 10a), and $|.|$ represents the absolute value. The dimensionless tidal component of the forcing (28), $\sin(2\pi t/\tau_L)\sin(2\pi t/\tau_S)$, is shown in figure 10a.

With a boundary layer velocity given by (28), the dimensionless coupled layered intrusion-melt equations become

$$\left(\frac{F^2}{h_1^3} - 1\right)\frac{\partial h_1}{\partial x} = \frac{F^2}{h_1^3}\left(1 + C\frac{h}{h - h_1}\right) - \left(S + \frac{\partial h}{\partial x}\right), \tag{29}$$

$$\frac{1}{M}\frac{\partial h}{\partial x} = \left|\frac{U_T}{U_\infty}\sin\left(\frac{2\pi t}{\tau_L}\right)\sin\left(\frac{2\pi t}{\tau_S}\right) + \frac{1}{h_1}\right|\left(1 - \frac{h_1}{h}\right), \tag{30}$$

with $h_1 = F^{2/3}$ at $x = 0$ and $h = h_1 = 1$ at $x = \ell(t)$ as before.

Figure 10b shows the intrusion distance $\ell(t)$ as a function of time (i.e. as in figure 2a, e of the main text) for different values of the tidal velocity, obtained by solving the coupled equations (29)–(30). We see that for tidal velocity amplitudes that are small relative to the far field velocity, $U_\mathrm{T}/U_\infty \ll 1$, the tidal influence is small and the system behaves as described in the main text for no tidal forcing. The tidal forcing component simply introduces oscillations about the 'no-tide' solution, on the tidal timescales. However, for relatively large tidal velocity amplitudes, $U_\mathrm{T}/U_\infty \gg 1$, the tidal signal dominates, demonstrating significantly enhanced intrusion distances compared to the case with no tidal influence.

It is possible to demonstrate that, even with the parametrization of tidal influence described above, the system displays the same tipping point like behaviour described in the main text for no tidal signal. In the no-tidal forcing case (section 2), we described how anaylsis of the steady form of the governing equations can be used to determine where in parameter space the tipping point occurs. With tidal forcing, however, no true steady state exists because the forcing is time-dependent. An approximation to the steady behaviour can be obtained by considering the large tidal amplitude limit, $U_{\mathrm{T}}/U_\infty \gg 1$, and the average over the monthly tidal cycle. This is equivalent to replacing (28) by

$$u^* = \lambda U_T, \tag{31}$$

where $\lambda \approx 0.405$ is the average of the function $|\sin(2\pi t/\tau_S)\sin(2\pi t/\tau_L)|$ over a monthly cycle. This is reasonable because the timescale on which the ice geometry responds to melting is relatively long compared to the timescale on which the tidal forcing varies. Figure 10b shows that this approximation works well (the red curve agrees fairly well with the yellow curves), although fails to capture short timescale oscillations, as is to be expected.

With a boundary layer velocity as given by (31), the steady form of the dimensionless coupled layered intrusion-melt equations read

$$\left(\frac{F^2}{h_1^3} - 1\right)\frac{\partial h_1}{\partial x} = \frac{F^2}{h_1^3}\left(1 + C\frac{h}{h - h_1}\right) - \left(S + \frac{\partial h}{\partial x}\right), \tag{32}$$

$$\frac{1}{M}\frac{\partial h}{\partial x} = \frac{\lambda U_T}{U_\infty}\left(1 - \frac{h_1}{h}\right). \tag{33}$$

We find that, as in the case of no tidal velocity, the tipping point exists and is generic: for any hydrological network efficiency F, the intrusion length increases with the melt parameter M and there is a critical M above which the intrusion becomes unbounded. Figure 10c shows the bounded-unbounded intrusion length transition for different values of U_T/U_∞ in the case $U_T/U_\infty \gg 1$. The data shown in this figure are obtained as described in section 2, but using the steady equations (32)–(33). The effect of the tidal velocity is to modify the location of the boundary between bounded and unbounded intrusions, with higher tidal velocities corresponding to a higher susceptibility to the unbounded regime.

4 Supplementary figures

References

[1] Robel, A. A., Wilson, E. & Seroussi, H. Layered seawater intrusion and melt under grounded ice. *The Cryosphere* **16**, 451–469 (2022).

[2] Wilson, E. A., Wells, A. J., Hewitt, I. J. & Cenedese, C. The dynamics of a subglacial salt wedge. *J. Fluid Mech.* **895** (2020).

[3] Hewitt, I. J. Subglacial plumes. *Annu. Rev. Fluid Mech.* **52**, 145–169 (2020).

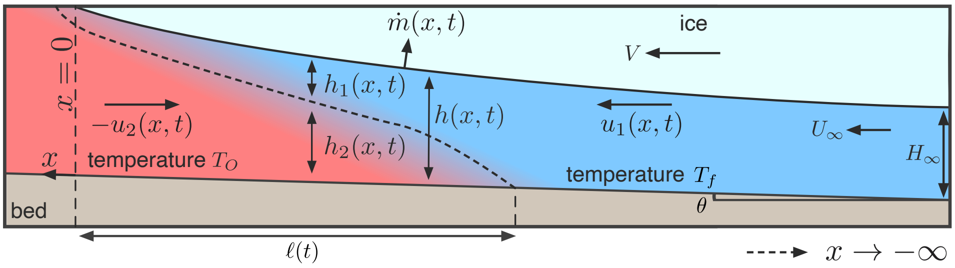

Supplementary Figure 1 Schematic diagram of the grounding zone model: warm, salty water of temperature T_O (red) is overlain by cold, fresh water (blue) at the local temperature T_f. The grey dashed curve indicates an approximation to the interface between the layers. Note that the vertical scale has been exaggerated for clarity.

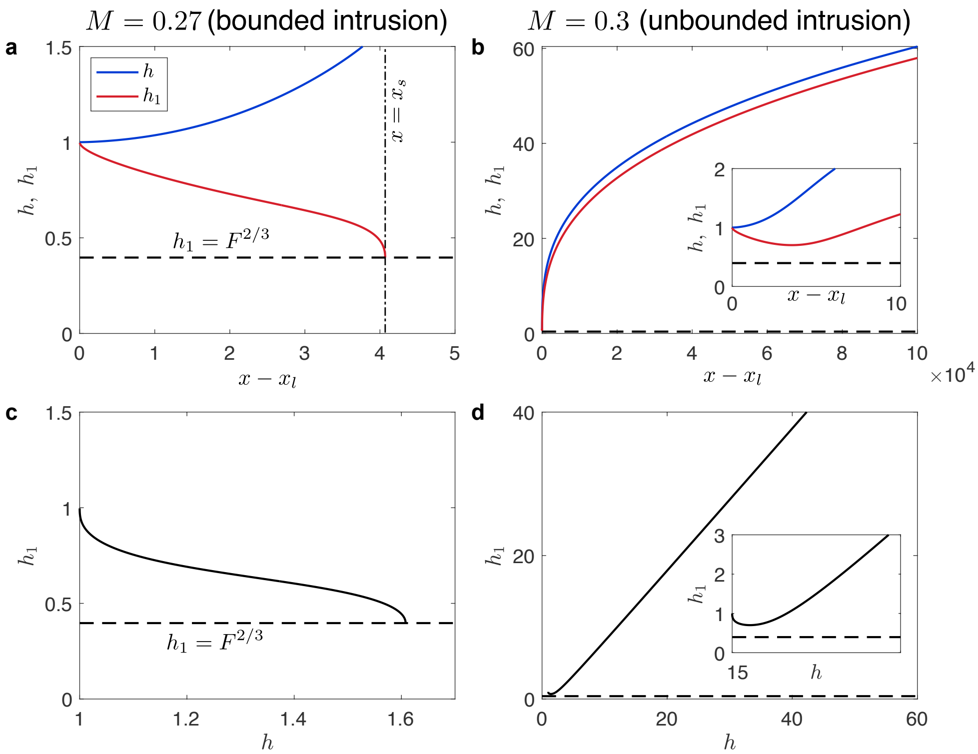

Supplementary Figure 2 Numerical solutions of the steady coupled intrusion-melt equations (24)–(25). Solutions are shown in (a–b) $(x - x_l, h)$ space and (c–d) (h, h_1) space. In each panel, the horizontal dashed line indicates the boundary condition $h_1 = F^{2/3}$, at which the solution would terminate, if it was attained. Results are shown for $M = 0.27$ (left-hand panels) and $M = 0.3$ (right-hand panels), corresponding to thermal forcing of 2.3°C and 2.5°C, respectively, as in figure 2 of the main text. These solutions are generated using a flat bed ($S = 0$), a fairly inefficient drainage system ($F = 0.25$), and $C = 0.1$. In (b) and (d), insets are as in the main panel, but zoomed in around the origin.

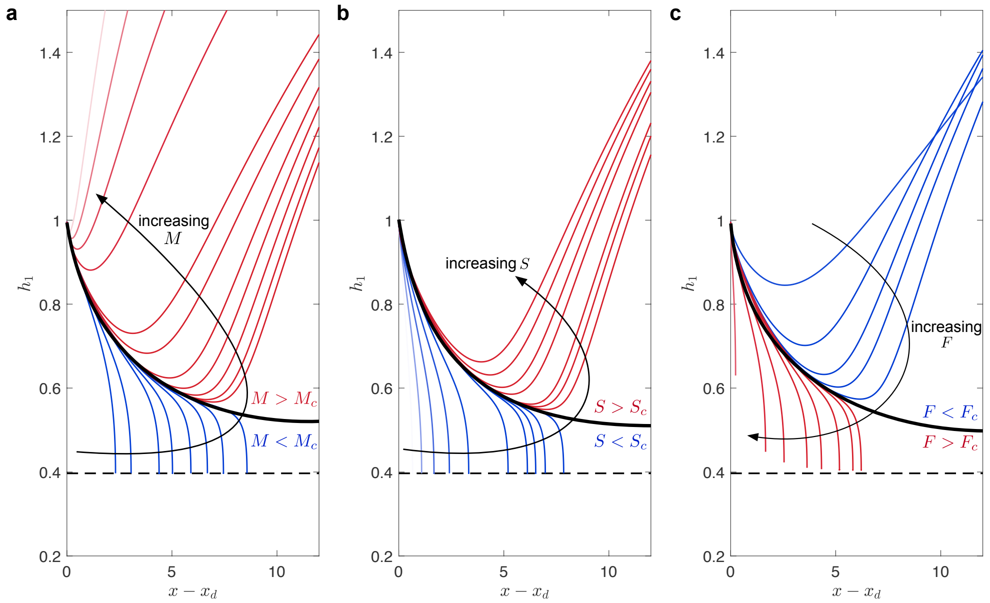

Supplementary Figure 3 Determining critical parameters for intrusion. Panels show h_1 as a function of $x - x_d$ for different values of (a) M, (b) S and (c) F. In each case, red (blue, respectively) curves indicate solution trajectories when the parameter is above (below) its continuous intrusion threshold, indicated with a subscript c (i.e. M_c, S_c, and F_c). Black curves indicate the solution trajectory with parameter values at the threshold.

[4] Jenkins, A. *et al.* Observations beneath pine island glacier in west antarctica and implications for its retreat. *Nat. Geosci* **3**, 468–472 (2010).

[5] Wells, A. J. & Worster, M. G. Melting and dissolving of a vertical solid surface with laminar compositional convection. *Journal of fluid mechanics* **687**, 118–140 (2011).

[6] Jenkins, A. Convection-driven melting near the grounding lines of ice shelves and tidewater glaciers. *J. Phys Oceanogr.* **41**, 2279–2294 (2011).

[7] Bradley, A. T., Rosie Williams, C., Jenkins, A. & Arthern, R. Asymptotic analysis of subglacial plumes in stratified environments. *Proc. R. Soc. Lond* **478**, 20210846 (2022).

[8] Gudmundsson, G. Ice-shelf buttressing and the stability of marine ice sheets. *The Cryosphere* **7**, 647–655 (2013).

[9] Padman, L., Siegfried, M. R. & Fricker, H. A. Ocean tide influences on the antarctic and greenland ice sheets. *Rev. Geophys.* **56**, 142–184 (2018).

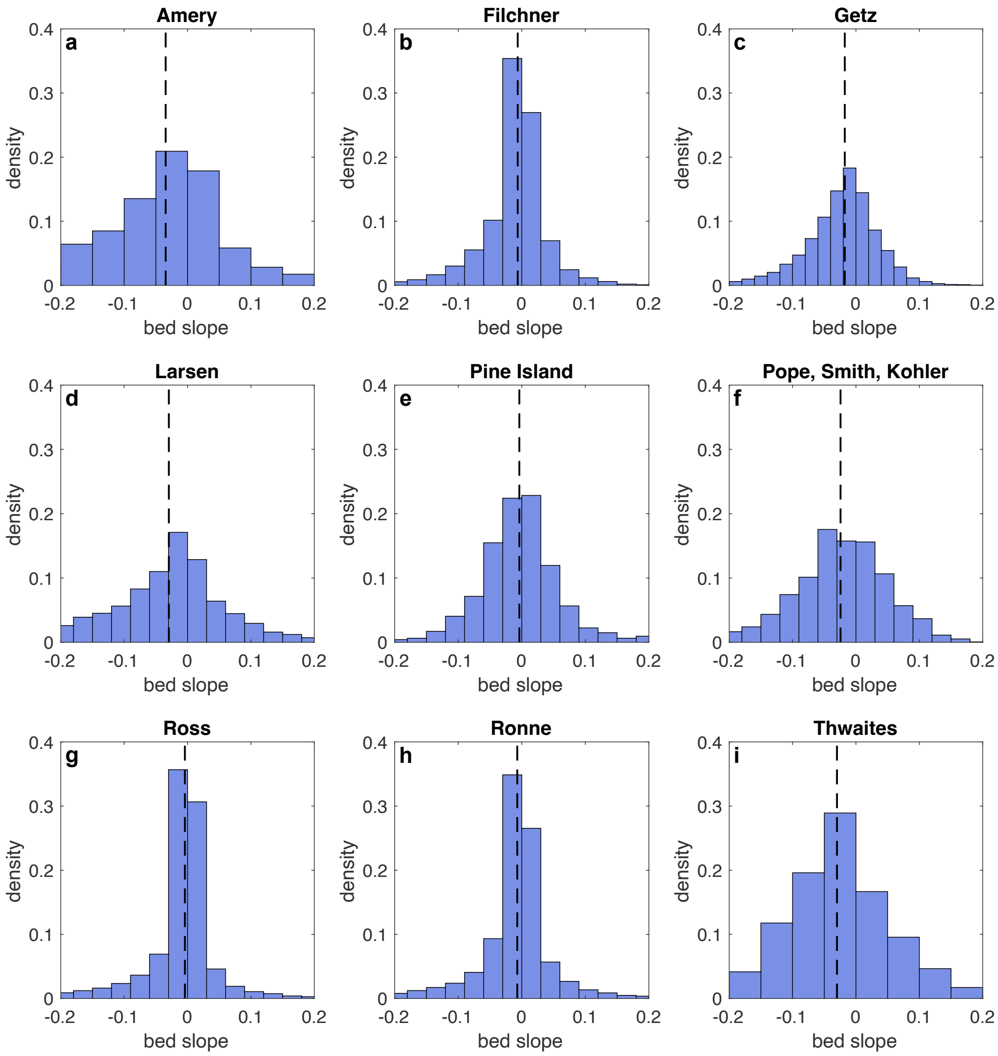

Supplementary Figure 4 Histograms of grounding line slope for key Antarctic ice-shelves. In each panel, the black dashed line indicates the median of the data showed therein.

[10] Freer, B. I., Marsh, O. J., Hogg, A. E., Fricker, H. A. & Padman, L. Modes of antarctic tidal grounding line migration revealed by icesat-2 laser altimetry. *The Cryosphere* 1–35 (2023).

[11] Warburton, K., Hewitt, D. & Neufeld, J. Tidal grounding-line migration modulated by subglacial hydrology. *Geophys. Res. Lett.* **47**, e2020GL089088 (2020).

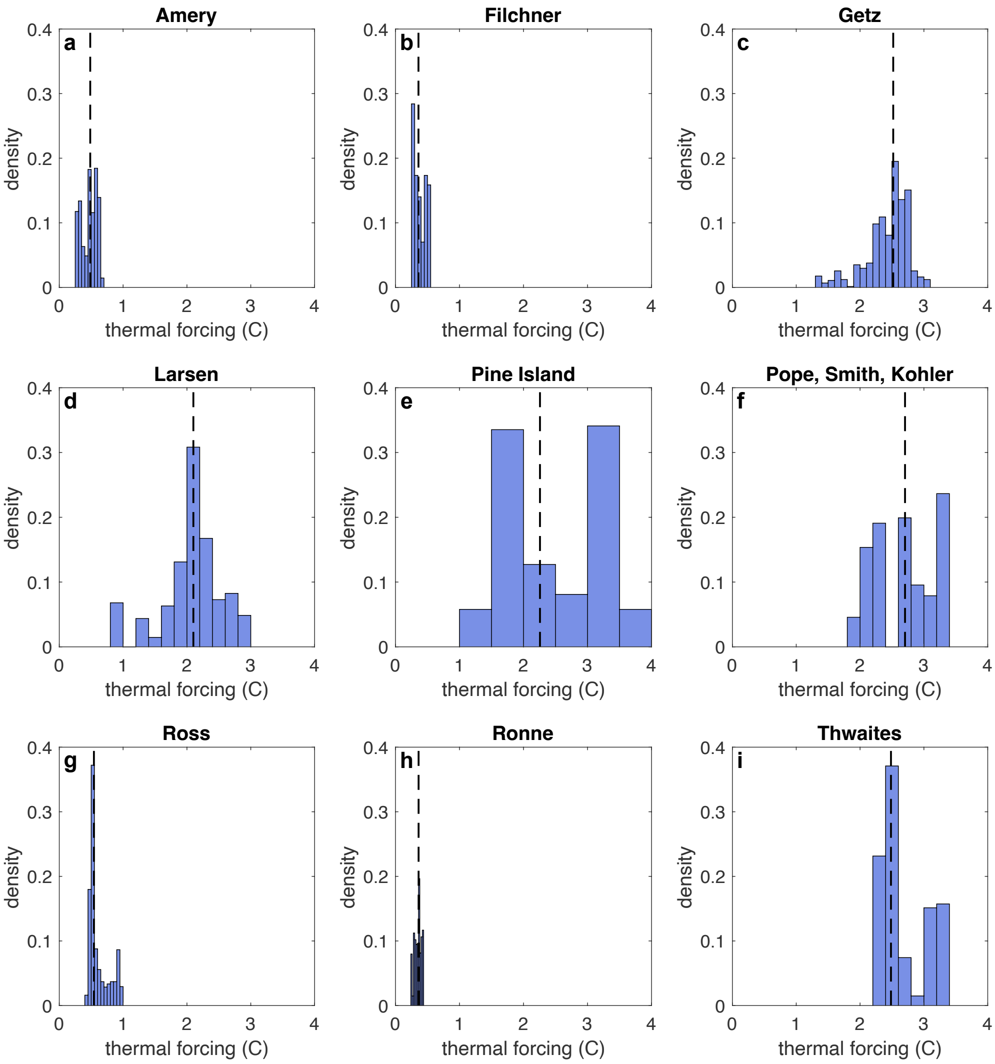

Supplementary Figure 5 Histograms of thermal driving for key Antarctic ice-shelves. In each panel, the black dashed line indicates the median of the data showed therein.

[12] Begeman, C. B. *et al.* Tidal pressurization of the ocean cavity near an antarctic ice shelf grounding line. *J. Geophys. Res. Oceans* **125**, e2019JC015562 (2020).

[13] Walker, R. T. *et al.* Ice-shelf tidal flexure and subglacial pressure variations. *Earth Planet. Sci. Lett.* **361**, 422–428 (2013).

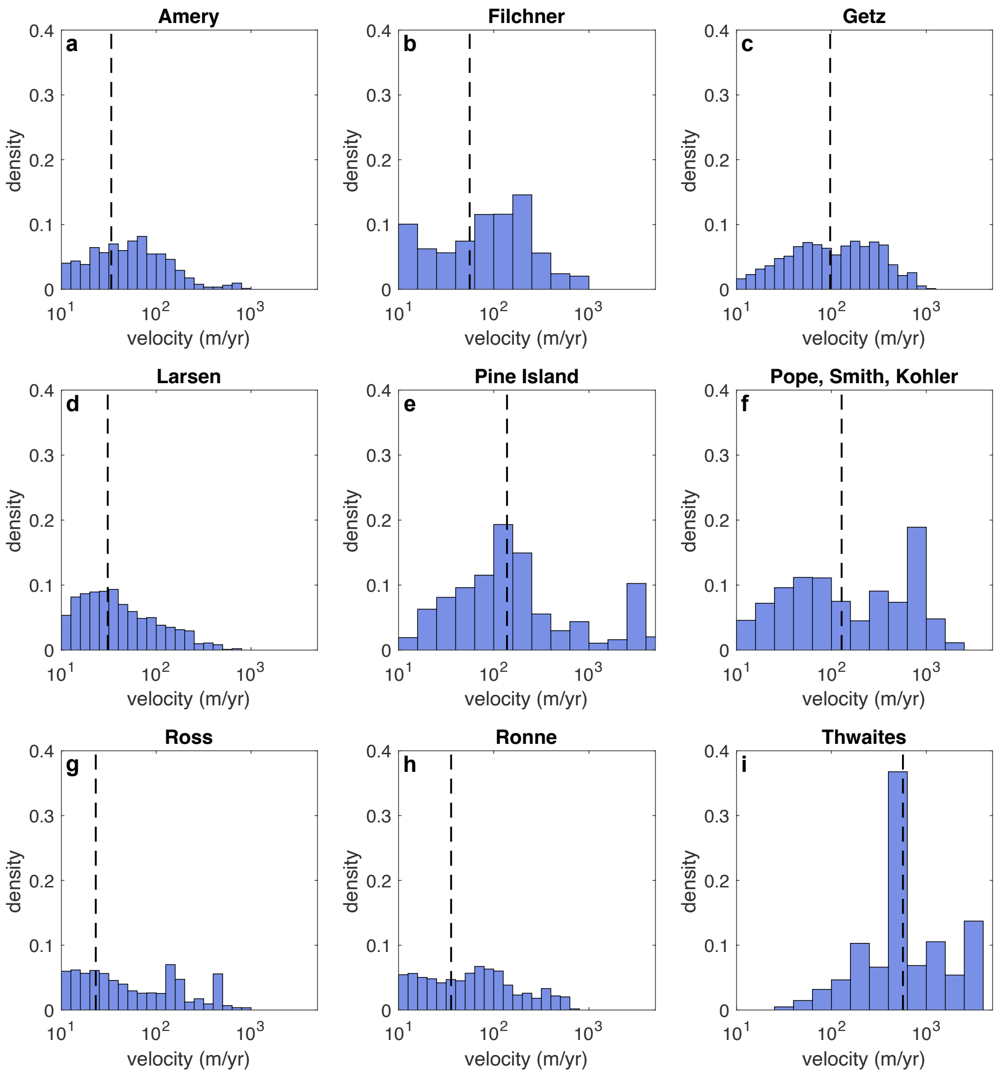

Supplementary Figure 6 Histograms of grounding line velocity for key Antarctic ice-shelves. In each panel, the black dashed line indicates the median of the data showed therein.

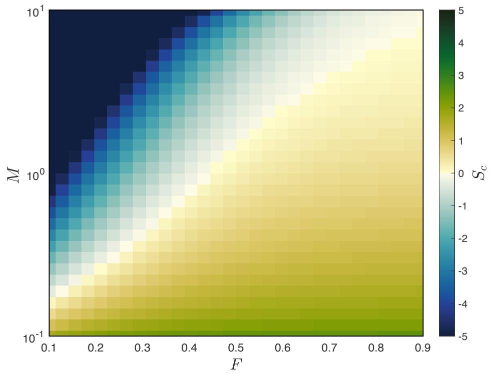

Supplementary Figure 7 Critical dimensionless slope for intrusion. Map of S_c as a function of dimensionless hydrological network efficiency F and melt parameter M.

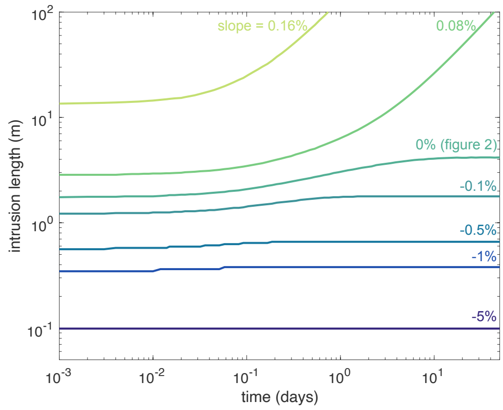

Supplementary Figure 8 Slope dependence of intrusion. Plots of time-dependent intrusion distance (i.e. that obtained by evolving from a configuration with initially parallel channel walls, as shown in figure 2a,e of the main text) for different basal slopes ($\tan\theta$), as labelled. Other parameters used to generate this plot correspond to the bounded intrusion case in figure 2 (which considers no slope), i.e. $F = 0.25$ and $C = 0.1$.

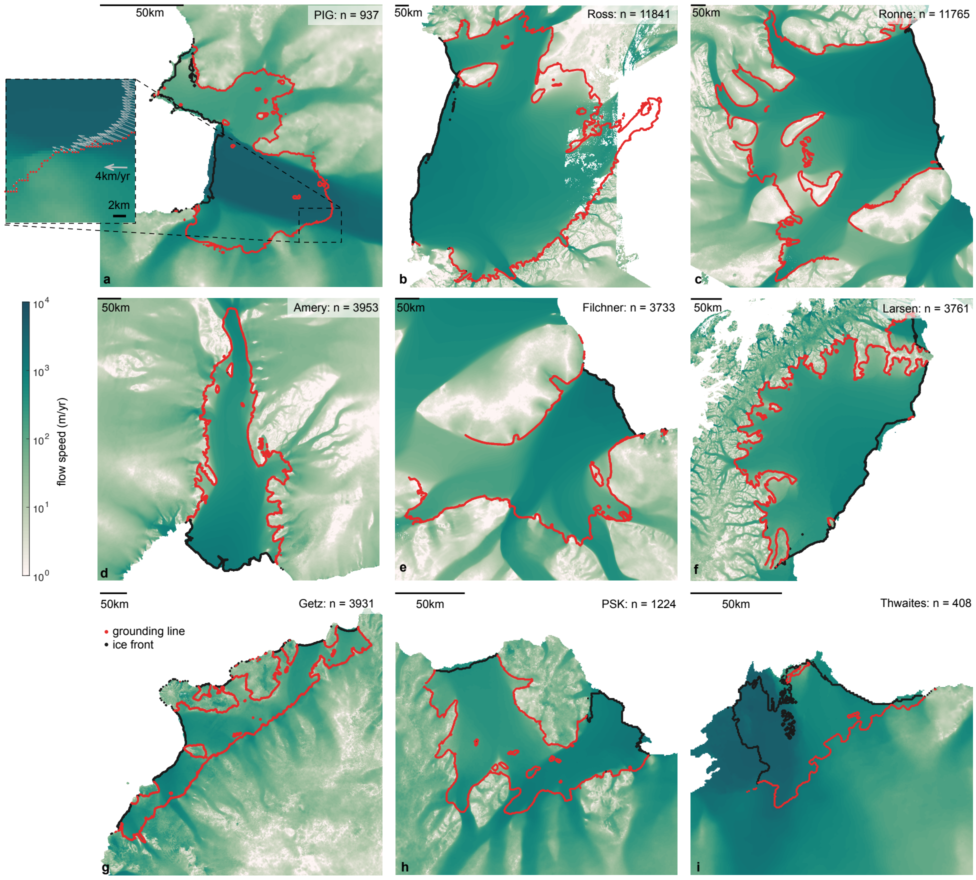

Supplementary Figure 9 Grounding line and ice front locations on key Antarctic ice shelves. Plots of ice velocity (colours) alongside locations of grounding line (red) and ice front (black) points for ice shelves considered in this study, as follows: (a) Pine Island Glacier, (b) Ross, (c) Ronne, (d) Amery, (e) Filchner, (f) Larsen, (g) Getz, (h) Pope, Smith, and Kohler, and (i) Thwaites. The inset in (a) shows the grounding line points alongside grounding line velocity vectors for the section within the box in the main panel. In each panel, the number n indicates the number of grounding line points included in the corresponding shelf.

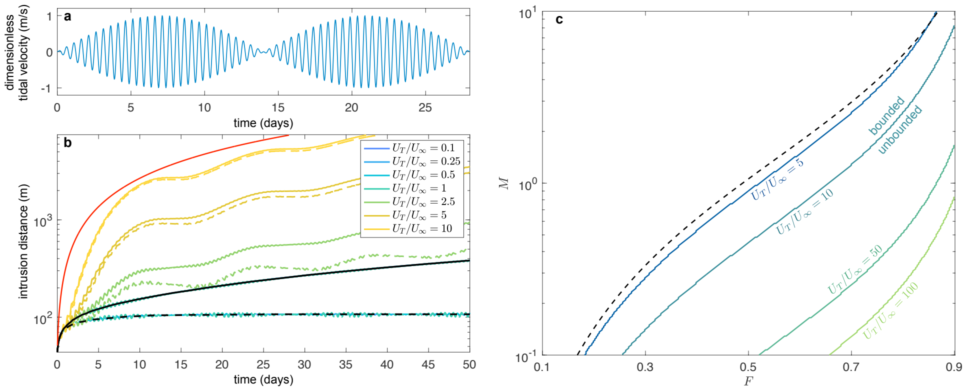

Supplementary Figure 10 Tidal modulation of seawater intrusions. (a) Dimensionless tidal velocity $\sin(2\pi t/\tau_L)\sin(2\pi t/\tau_S)$ as a function of time. (b) Intrusion length $\ell(t)$ as a function of time (i.e. not the final intrusion length, but as in figure 2a, e of the main text) for different values of the reduced tidal velocity U_T/U_∞ as indicated by the colourbar. Data here are shown in dimensional form to allow comparison with figure 2 of the main text. For each value of U_T/U_∞, results are shown for the two cases shown in figure 2 of the main text, with $\Delta T = 2.3°\mathrm{C}$ (dashed lines) and $\Delta T = 2.5°\mathrm{C}$ (solid lines). Black solid and dashed curves show results obtained with no tides, i.e. as shown in figure 2 of the main text. Note that the curves corresponding to $U_T/U_\infty \lesssim 0.5$ are indistinguishable from the black curves. The red curve indicates the intrusion length for the approximate case, where the boundary layer velocity is given by the average over a monthly cycle (equation (31)). Other parameters are as in figure 2 of the main text. (c) Coloured contours show the boundary between bounded and unbounded intrusions for different values of U_T/U_∞ as labelled. Labels 'bounded' and zunbounded' indicate which side of the line corresponds to bounded and unbounded intrusions for the $U_T/U_\infty = 10$ case. The black dashed contour indicates the '$C = 0.1$' of figure 3 of the main text, corresponding to no tidal influence.